High-Resolution Spectral and Anisotropy Characteristics of Solar Protons During the GLE N°73 on 28 October 2021 Derived with Neutron-Monitor Data Analysis

Alexander L. Mishev[1,2] ⓘ · Leon G. Kocharov[2] · Sergey A. Koldobskiy[1,2] ·
Nicholas Larsen[2] · Esa Riihonen[3] · Rami Vainio[3] · Ilya G. Usoskin[1,2]

Abstract
The first ground-level enhancement of the current Solar Cycle 25 occurred on 28 October 2021. It was observed by several space-borne and ground-based instruments, specifically neutron monitors. A moderate count-rate increase over the background was observed by high-altitude polar stations on the South Pole and Dome C stations at the Antarctic plateau. Most of the neutron monitors registered only marginal count-rate increases. Using detrended records and employing a method verified by direct space-borne measurements, we derive the rigidity spectra and angular distributions of the incoming solar protons in the vicinity of Earth. For the analysis, we employed a newly computed and parameterized neutron-monitor yield function. The rigidity spectra and anisotropy of solar protons were obtained in their time evolution throughout the event. A comparison with the Solar and Heliospheric Observatory/Energetic and Relativistic Nuclei and Electron (SOHO/ENRE) experiment data is also performed. We briefly discuss the results derived from our analysis.

✉ A.L. Mishev
   alexander.mishev@oulu.fi; alex_mishev@yahoo.com

L.G. Kocharov
leon.kocharov@oulu.fi

S.A. Koldobskiy
sergey.koldobskiy@oulu.fi

N. Larsen
nicholas.larsen@oulu.fi

E. Riihonen
riihonen@utu.fi

R. Vainio
rami.vainio@utu.fi

I.G. Usoskin
ilya.usoskin@oulu.fi

1   Space Physics and Astronomy Research Unit, University of Oulu, Oulu, Finland

2   Sodankylä Geophysical Observatory, University of Oulu, Oulu, Finland

3   Department of Physics and Astronomy, University of Turku, Turku, Finland

⚛ Springer

1. Introduction

Eruptive processes on the Sun, e.g., flares and/or coronal mass ejections, result in solar energetic particle (SEP) events, that is, distinct enhancements of fluxes of protons, heavy ions and electrons (e.g. Aschwanden, 2012; Desai and Giacalone, 2016; Klein and Dalla, 2017, and references therein). The most energetic SEP events can last from hours to up to several days (Moraal and McCracken, 2012; Vainio et al., 2009, 2013; Gopalswamy et al., 2014; Raukunen et al., 2018; Usoskin et al., 2020). The energy of SEPs in most cases is in the MeV range, yet in some cases, accelerated protons can gain energy up to the GeV energy range.

A study of SEP properties provides a unique basis to reveal important processes of both SEP acceleration on the Sun and their propagation in the interplanetary space (e.g. Debrunner et al., 1988; Reames, 1999; Gopalswamy et al., 2014; Kocharov et al., 2021). A specific interest is paid to relatively rare events, with SEP energy reaching about GeV/nucleon or even greater values. Solar protons with energy above 300 MeV/nucleon can produce secondary particles in the Earth's atmosphere reaching the ground by generating an atmospheric cascade, whose byproducts are eventually registered by ground-based detectors, e.g., neutron monitors (NMs) (e.g. Dorman, 2004; Kühl et al., 2017; Mishev and Poluianov, 2021, and references therein). This class of events is called ground-level enhancements (GLEs) (for details see Shea and Smart, 1982; Poluianov et al., 2017).

The current paradigm of ground level enhancements (GLEs) is that most likely they represent the high-energy tail of SEPs and are related to both solar flares and CMEs (e.g. Cliver, 2016; Desai and Giacalone, 2016; Miroshnichenko, 2018; Anastasiadis et al., 2019; Kocharov et al., 2020, and references therein). GLEs can be conveniently studied with ground-based and space-borne instruments (e.g. Bieber and Evenson, 1995; Simpson, 2000; Bruno et al., 2018), yet the latter usually orbit most of the time in high-rigidity cut-off regions, therefore being not full-time sensitive to the SEPs, whilst the former, specifically high-altitude polar instruments are sensitive to solar protons with energy of about 300 MeV/nucleon (e.g. Mishev and Poluianov, 2021).

On the other hand, GLEs can be registered and studied using the worldwide NM network (Simpson, Fonger, and Treiman, 1953; Hatton, 1971; Stoker, Dorman, and Clem, 2000; Mavromichalaki et al., 2011; Papaioannou et al., 2014), that is, stations located at different geographic regions are sensitive to a different part of the SEP spectra and arrival direction so that using the geomagnetosphere as a spectrometer, one can reveal their characteristics (e.g. Bieber and Evenson, 1995). At present, 73 GLEs have been registered, the first to the fifth by ionization chambers. Starting from GLE N°5, their registration is carried out by NMs, and the records are stored in the International GLE Database (IGLED) (https://gle.oulu.fi, for details see Usoskin et al., 2020).

GLEs occur sporadically and differ from each other in the shape of the spectra, particle flux, angular distribution, duration, as well as time evolution of their characteristics (e.g. Moraal and McCracken, 2012; Raukunen et al., 2018; Koldobskiy et al., 2021). Therefore, GLEs are studied case-by-case, yet some common features have been recently reported (Kocharov et al., 2015, 2018). Here, we investigate the most recent GLE, namely, GLE N°73 registered on 28 October 2021 (e.g. Papaioannou et al., 2022; Velinov, 2022), and present the rigidity spectra and angular distribution of SEPs, including their dynamical evolution throughout the event, employing NM data analysis.
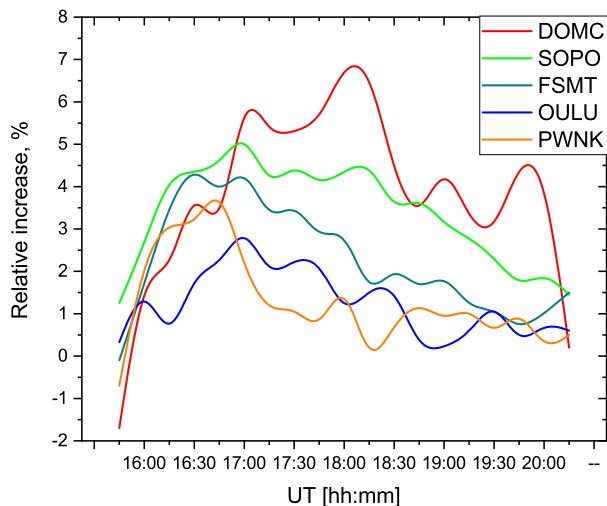
2. GLE N°73 on 28 October 2021

The first GLE event of the current Solar Cycle 25 was observed on 28 October 2021 as a weak increase (below 20% with respect to the galactic cosmic-ray (GCR) background) by several NMs, specifically those located in the low-rigidity cut-off region and several space-borne instruments (for details see Papaioannou et al., 2022). The 28 October 2021 event is associated with a gradual, class X1.0 flare located at S28W01, with peak of soft X-ray emission at 15:35 UT, and an asymmetric halo coronal mass ejection (CME), brightest over the southern hemisphere of the Sun according to the Large Angle and Spectrometric Coronagraph (LASCO) C2 observations (SOHO/LASCO C2; Brueckner et al., 1995).

In Figure 1 we present the detrended NM count-rate increases registered by several selected stations during the event. We note that detrended data account for the GCR baseline temporal variability, specifically the contribution of short-time variations of GCRs, most likely due to transients and local anisotropy. Therefore, the detrended data provide smooth and free from transients, including diurnal variations, records of NM count-rate increases due to SEPs (for details see Usoskin et al., 2020).

The peak count-rate increase was registered by low-rigidity cut-off, high-altitude polar NMs, namely those located at the South Pole and French–Italian Dome C (Concordia) research stations, South Pole (SOPO) (5.4%) and South Pole Bare (SOPB) (5.7%), DOMC (7.3%) and DOMB (14%), standard and bare monitors, respectively (see Table 1). The high-altitude polar NMs have greater sensitivity in energy to SEPs compared to the sea-level ones because of the reduced atmospheric attenuation, namely about 300 MeV/nucleon for the former and about 430 MeV/nucleon for the latter (for details see Mishev and Poluianov, 2021, and the discussion therein). In addition, bare NMs are more sensitive to the low-energy part of the GLE-producing SEPs (e.g. Clem and Dorman, 2000; Vashenyuk, Balabin, and Stoker, 2007; Nuntiyakul et al., 2018, 2020).

Several NM stations observed the event onset at about 15:50 UT (e.g. SOPO and Fort Smith (FSMT)). The event lasted for about 4.5 h, however, the statistically significant signal registered by a sufficient number of NMs, allowing reliable data analysis (see the discussion in Mishev and Usoskin, 2020), was observed from about 16:00 UT to about 20:00 UT. The event revealed a slow, gradual increase of NM count rates and moderate anisotropy, that is

the angular distribution width $\sigma^2 \approx \pi$, similarly to the event(s) described by Bombardieri et al. (2006) as opposed to very anisotropic events described by Bütikofer et al. (2009). The event occurred on the background of a strong diurnal wave caused by the local anisotropy of GCRs, accordingly, the background was detrended and averaged over two hours before the event onset employing the procedure described in Usoskin et al. (2020). For the data analysis, we consider five-minute integrated detrended records of the NM count-rate increases available at the IGLED. Here, we emphasize that the one-minute records of the NM count-rate increases depicted considerably larger fluctuations, not allowing strictly precise data analysis, yet some estimations are presented below.

3. Analysis of the Neutron-Monitor Data

In this section, we employ a method and model for an analysis of the NM data, based on the algorithm initially developed by Shea and Smart (1982), Cramp et al. (1997), Vashenyuk et al. (2006), Bombardieri et al. (2007). The details and applications are given elsewhere (Mishev and Usoskin, 2016; Mishev, Poluianov, and Usoskin, 2017; Mishev et al., 2018, 2021a). The data analysis of the NM records allowing us to derive SEP spectra, angular distribution, and apparent source position, is based on modeling the response of the global NM network and optimization of the modeled over the experimental data, assuming an appropriate initial guess (Cramp, Humble, and Duldig, 1995).

The method initially developed by our team (e.g. Mishev, Kocharov, and Usoskin, 2014) was recently improved and verified by direct space-borne measurements (for details see Koldobskiy et al., 2019a; Mishev et al., 2021b; Koldobskiy et al., 2021). In this article, we perform the modeling using a newly computed and verified, altitude-dependent NM yield function (Mishev et al., 2020), which depicted reasonable latitude and altitude surveys, and space-borne records by PAMELA (Payload for Antimatter Matter Exploration and Light-nuclei Astrophysics, Adriani et al., 2017) and AMS-02 (Alpha Magnetic Spectrometer, Aguilar et al., 2021) (for details see the discussions in Lara, Borgazzi, and Caballero-Lopez, 2016; Nuntiyakul et al., 2018; Koldobskiy et al., 2019b). We benefit from the employment of stations located at different altitudes as well as the pairs of standard and bare NMs (South Pole and Dome C) (for details, see e.g., Ruffolo et al., 2006; Bieber et al., 2013). In addition, the optimization by Aleksandrov (1971), Golub and Van Loan (1980), Golub, Hansen, and O'Leary (1999), Mishev, Mavrodiev, and Stamenov (2005) to the Levenberg–Marquardt (Levenberg, 1944; Marquardt, 1963) algorithm used in this work, allowed us to reduce unfolding uncertainties and obtain a reliable solution even in the case of ill-posed problem(s), arising from the weak and fluctuated NM responses (e.g., see the discussions in Tikhonov et al., 1995; Mavrodiev, Mishev, and Stamenov, 2004; Aster, Borchers, and Thurber, 2005; Mishev et al., 2021b).

The merit function ($\mathcal{D}$ in Equation 1) that is the main criterion for the quality of the fit, represents the residual (Himmelblau, 1972; Dennis and Schnabel, 1996):

$$\mathcal{D} = \frac{\sqrt{\sum_{i=1}^{m} \left[\left(\frac{\Delta N_i}{N_i} \right)_{\text{mod.}} - \left(\frac{\Delta N_i}{N_i} \right)_{\text{meas.}} \right]^2}}{\sum_{i=1}^{m} (\frac{\Delta N_i}{N_i})_{\text{meas.}}}, \tag{1}$$

simultaneously including additional criteria as discussed in Mishev et al. (2021a,b). In Equation 1, ΔN_i, corresponds to the difference between the modeled and recorded count-rate increases of the ith NM, and N_i to the nominal count-rate increase of the ith NM. Whilst

$\mathcal{D} \leq 5\%$ for strong events (e.g., see Vashenyuk et al., 2006), for weak events it is normally $\approx 10-15\%$, and in some cases about 20% (e.g. Mishev et al., 2018).

In our model, we can imply a spectral approximation with a modified power-law or an exponential rigidity spectrum as in Cramp et al. (1997), Vashenyuk et al. (2008), Mishev et al. (2021b).

The analytical expression of the rigidity spectrum of SEPs with rigidity $P > 1$ GV given by a modified power law is:

$$J_{\parallel}(P) = J_0 P^{-(\gamma + \delta\gamma(P-1))}, \tag{2}$$

where the flux of particles with rigidity P in [GV] is along the axis of symmetry identified by geographic latitude Ψ and longitude Λ and the power-law exponent is γ with the steepening of $\delta\gamma$, J_0 is the particle flux at 1 GV in [m^{-2} s^{-1} sr^{-1} GV^{-1}]. At $P \leq 1$ GV, the rigidity spectrum of SEPs is approximated with:

$$J_{\parallel}(P) = J_0 P^{-(\gamma + \delta\gamma \cdot P)}. \tag{3}$$

The exponential shape is described by the expression:

$$J_{\parallel}(P) = J_0 \exp(-P/P_0), \tag{4}$$

where P_0 is a characteristic proton rigidity in [GV].

The pitch-angle distribution (PAD) was assumed to be a Gaussian-like distribution:

$$G(\alpha(P)) \sim \exp(-\alpha^2/\sigma^2), \tag{5}$$

where α is the pitch angle, σ accounts for the width of the distribution.

The propagation of SEPs in the geomagnetosphere, necessary for the computation of the rigidity cut-offs and asymptotic directions of the NMs selected for the analysis (Cooke et al., 1991), is performed implying a superposition of the International Geomagnetic Reference Field (IGRF) geomagnetic model (epoch 2020) as the internal field model (Alken et al., 2021) and the Tsyganenko-89 model as the external field (Tsyganenko, 1989), which assures straightforward and reasonably accurate modeling of SEPs propagation in the Earth's magnetosphere (Kudela and Usoskin, 2004; Kudela, Bučik, and Bobik, 2008; Nevalainen, Usoskin, and Mishev, 2013). The NM stations used for our analysis with their standard acronyms, rigidity cut-offs (P_c), geographic coordinates, altitudes above the sea level, and the type of the instrument are given in Table 1.

4. Results of the Analysis

Before the unfolding of the NM records, we computed the rigidity cut-offs and asymptotic directions for all NMs from Table 1. An example of NM asymptotic directions in the rigidity range $1-5$ GV, corresponding to the rigidity cut-off of the station and encompassing maximal NM response (DOMC and SOPO are plotted in the range $0.7-5$ GV), is presented in Figure 2, while in the analysis we considered the $1-20$ GV rigidity range.

Subsequently, we examine all possibilities in our model as spectral and PAD functional shapes, that is, by modified power law or exponential rigidity spectra of SEPs (Equations 2–4), as well as by Ellison and Ramaty (1985) spectral form.

The best fit is obtained using a modified power-law rigidity spectrum of SEPs and single-Gaussian PAD, depicted for various stages of the event in Figure 3, the details are presented

Table 1 Neutron monitors with standard acronyms, geographic coordinates (latitude and longitude), rigidity cut-off, altitude above the sea level, and type of instrument used for the analysis of GLE N°73.

Station	Latitude [deg]	Longitude [deg]	P_c [GV]	Altitude [m]	Type
Alma Aty (AATY)	43.25	76.92	6.67	3340	18NM-64
Apatity (APTY)	67.55	33.33	0.48	177	18NM-64
Athens (ATHN)	37.98	23.78	8.42	260	6NM-64
Baksan (BKSN)	43.28	42.69	5.6	1700	6NM-64
Calgary (CALG)	51.08	245.86	1.08	1128	12NM-64
Dome C (DOMC)	−75.06	123.20	0.1	3233	standard mini
Dome C bare (DOMB)	−75.06	123.20	0.1	3233	bare mini
Dourbes (DRBS)	50.1	4.6	3.34	225	12NM-64
Fort Smith (FSMT)	60.02	248.07	0.25	0	18NM-64
Inuvik (INVK)	68.35	226.28	0.16	21	18NM-64
Jang Bogo (JNBG)	−74.37	164.13	0.1	29	5NM-64
Jungfraujoch (JUN1)	46.55	7.98	4.46	3476	3NM-64
Kerguelen (KERG)	−49.35	70.25	1.01	33	18NM-64
Lomnicky Štit (LMKS)	49.2	20.22	3.72	2634	12NM-64
Mexico city (MXCO)	19.33	260.8	7.59	2274	6NM-64
Nain (NAIN)	56.55	298.32	0.28	0	18NM-64
Norilsk (NRLK)	69.26	88.05	0.58	0	18NM-64
Oulu (OULU)	65.05	25.47	0.69	15	9NM-64
Peawanuck (PWNK)	54.98	274.56	0.16	52	18NM-64
Rome (ROME)	41.9	12.52	6.11	60	18NM-64
Sanae (SNAE)	−70.3	357.65	0.73	52	6NM-64
South Pole (SOPO)	−90.00	0.0	0.01	2820	3NM-64
South Pole (SOPB)	−90.00	0.0	0.01	2820	bare 6NM-64
Terre Adelie (TERA)	−66.67	140.02	0	45	9NM-64
Thule (THUL)	76.60	291.2	0.1	260	9NM-64
Tixie Bay (TXBY)	71.60	128.90	0.53	0	18NM-64
Yakutsk (YKTK)	62.01	129.43	1.65	105	18NM-64

in Table 2. The angular distribution of SEPs derived in this case is simpler than that of the two previous GLEs (Mishev, Kocharov, and Usoskin, 2014; Adriani et al., 2017; Mishev et al., 2021b).

An analysis of 1-min records, available in the NM database (Mavromichalaki et al., 2011), was also performed during the event onset. We note that, in this case, considerably larger fluctuations in NM count rates resulted in greater residuals, therefore not all fit-quality criteria were fulfilled (for details see the discussion in Mishev et al., 2021a). However, we present the results of this analysis in Table 3, which are important in relation to particle-acceleration studies (e.g. Klein and Trottet, 2001, and references therein).

The derived SEP spectra are moderately hard, slightly softer compared to the previous two weak events: GLE N°71 and GLE N°72 (Plainaki et al., 2014; Adriani et al., 2017; Mishev et al., 2018; Bruno et al., 2018, 2019; Mishev et al., 2021a). The SEP spectra revealed an important steepening, with considerable roll-off, significantly greater than that of GLE N°71 and GLE N°72 (Mishev et al., 2018, 2021a). The spectra slowly and steadily softened throughout the event, accordingly, the steepening decreased and vanished in the

Table 2 Derived spectral and angular characteristics during GLE N°73 on 28 October 2021 fitted with a modified power-law rigidity spectrum. The columns correspond to the integration interval (1), particle flux (2), spectrum slope (3), steepening of the spectrum (4), width of the angular distribution (5), anisotropy axis position (6,7), merit function $\mathcal{D}$ (8), and normalized to degrees of freedom χ_r^2 (9).

| Integration interval UT	J_0 [m^{-2} s^{-1} sr^{-1} GV^{-1}]	γ	$\delta\gamma$	σ^2 [rad^2]	Ψ [degrees]	Λ [degrees]	$\mathcal{D}$ [%]	χ_r^2
15:55 – 16:00	7.5e4	4.1	1.3	2.7	−10.0	−124.0	22	1.3
16:00 – 16:05	7.7e4	4.2	1.2	2.8	−12.0	−127.0	21	1.3
16:05 – 16:10	7.89e4	4.2	1.1	2.8	−13.0	−128.0	23	1.3
16:10 – 16:15	8.1e4	4.3	0.9	2.9	−14.0	−130.0	19	1.2
16:15 – 16:20	8.2e4	4.3	0.8	2.9	−15.0	−131.0	14	1.2
16:20 – 16:25	8.75e4	4.4	0.8	3.0	−21.0	−132.0	12	1.15
16:25 – 16:30	9.1e4	4.4	0.8	3.1	−30.0	−132.0	11	1.1
16:30 – 16:35	9.4e4	4.5	0.8	3.1	−34.0	−135.0	7.0	1.0
16:35 – 16:40	9.48e4	4.7	0.75	3.2	−31.0	−137.0	9.0	0.99
16:40 – 16:45	9.58e4	4.8	0.7	3.3	−35.0	−140.0	8.0	0.95
16:45 – 16:50	9.67e4	4.9	0.6	3.5	−38.0	−140.0	12	1.1
16:50 – 16:55	9.85e4	5.1	0.5	3.7	−37.0	−142.0	11	1.1
16:55 – 17:00	1.01e5	5.3	0.5	3.9	−40.0	−145.0	12	1.15
17:00 – 17:05	1.038e5	5.5	0.4	4.2	−50.0	−148.0	10	1.1
17:05 – 17:10	1.05e5	5.5	0.4	4.2	−50.0	−148.0	10	1.1
17:10 – 17:15	1.06e5	5.5	0.4	4.2	−48.0	−147.0	12	1.2
17:15 – 17:20	1.08e5	5.6	0.37	4.2	−50.0	−148.0	11	1.1
17:20 – 17:25	1.112e5	5.7	0.36	4.3	−52.0	−148.0	9.0	1.05
17:25 – 17:30	1.134e5	5.75	0.35	4.4	−54.0	−150.0	10	1.1
17:30 – 17:35	1.148e5	5.8	0.35	4.5	−57.0	−151.0	11	1.1
17:35 – 17:40	1.152e5	5.9	0.35	4.7	−61.0	−151.0	12	1.15
17:40 – 17:45	1.171e5	6.0	0.3	4.9	−54.0	−152.0	11	1.1
17:45 – 17:50	1.192e5	6.1	0.3	5.1	−55.0	−153.0	12	1.1
17:50 – 17:55	1.21e5	6.25	0.3	5.3	−52.0	−151.0	10	1.1
17:55 – 18:00	1.241e5	6.3	0.3	5.3	−57.0	−154.0	13	1.2
18:00 – 18:05	1.25e5	6.3	0.3	5.3	−58.0	−155.0	11	1.1
18:05 – 18:10	1.27e5	6.4	0.25	5.5	−54.0	−157.0	12	1.1
18:10 – 18:15	1.29e5	6.5	0.2	5.7	−52.0	−157.0	11	1.1
18:15 – 18:20	1.314e5	6.5	0.2	5.9	−55.0	−158.0	13	1.15
18:20 – 18:25	1.25e5	6.6	0.2	6.1	−50.0	−160.0	10	1.1
18:25 – 18:30	1.21e5	6.7	0.2	6.3	−45.0	−161.0	9.0	1.05
18:30 – 18:35	1.15e5	6.9	0.2	6.5	−42.0	−162.0	12	1.2
18:35 – 18:40	1.11e5	7.0	0.15	6.7	−37.0	−162.0	10	1.1
18:40 – 18:45	1.074e5	7.0	0.15	6.9	−33.0	−165.0	11	1.15
18:45 – 18:50	1.032e5	7.1	0.15	7.3	−31.0	−166.0	12	1.2
18:50 – 18:55	1.01e5	7.1	0.1	7.5	−27.0	−167.0	13	1.2
18:55 – 19:00	1.0e5	7.2	0.1	7.7	−24.0	−168.0	12	1.2
19:00 – 19:15	9.5e4	7.3	0.0	7.7	−20.0	−168.0	11	1.2
19:15 – 19:30	9.3e4	7.5	0.0	7.9	−24.0	−171.0	10	1.2
19:30 – 19:45	9.1e4	7.6	0.0	8.1	−27.0	−173.0	12	1.25
19:45 – 20:00	8.5e4	7.7	0.0	8.3	−18.0	−175.0	13	1.3
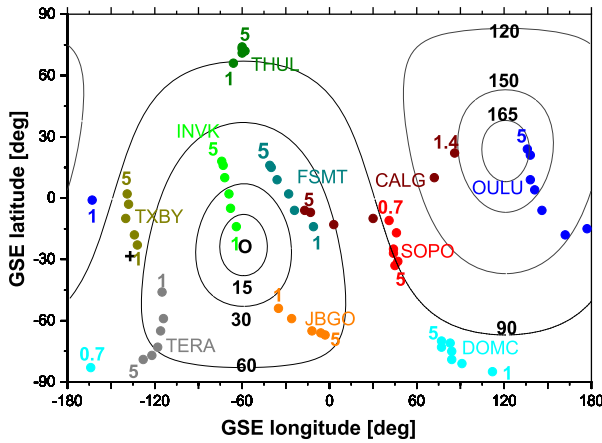
Figure 2 Asymptotic directions of selected NM stations during GLE N°73 on 28 October 2021 at 16:00 UT. The colored dots and numbers indicate the NM stations and asymptotic directions, with the standard acronyms given in Table 1. The small circle depicts the derived apparent source position, and the cross the interplanetary magnetic field (IMF) direction obtained by the Advanced Composition Explorer (ACE) satellite. The lines of equal pitch angles relative to the derived anisotropy axis are plotted for 15°, 30°, 60°, and 90° for sunward directions, and 120°, 150°, and 165° for anti-Sun directions.
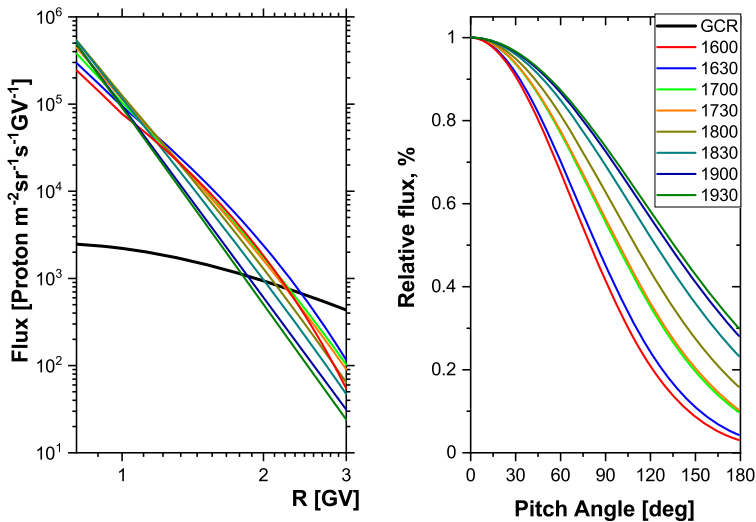
Figure 3 Derived rigidity *R* [GV] spectra (left panel) and PAD (right panel) during various stages of GLE N° 73 on 28 October 2021 as denoted in the legend, details are given in Table 2. The solid black line on the left panel depicts the GCR particle flux computed with the force-field model at a period corresponding with the occurrence of the event. Time [UT] corresponds to the start of the five-minute interval over which the data are integrated.

late phase, which was after 19:00 UT. The PAD was wider compared to beam-like events such as GLE N°69 and GLE N°70 (for details see Bütikofer et al., 2009) and broadened out during the event. In addition, it was not complicated, in contrast to GLE N°71 or GLE N°72, where Sun–anti-Sun SEP flux was observed (e.g. Adriani et al., 2015; Mishev et al., 2021a).

Table 3 Derived spectral and angular characteristics with 1-minute time resolution during the event onset of GLE N° 73.

Integration interval UT	J_0 [m^{-2} s^{-1} sr^{-1} GV^{-1}]	γ	$\delta\gamma$	σ^2 [rad^2]	Ψ [degrees]	Λ [degrees]	$\mathcal{D}$ [%]	χ_r^2
15:55 – 15:56	7.1e4	3.9	1.5	2.1	−10.0	−124.0	28	1.5
15:56 – 15:57	7.2e4	4.0	1.5	1.8	−10.0	−124.0	29	1.6
15:57 – 15:58	7.6e4	4.0	1.4	2.0	−12.0	−125.0	32	1.7
15:58 – 15:59	7.4e4	4.1	1.2	2.7	−8.0	−124.0	27	1.5
15:59 – 16:00	7.5e4	4.3	1.3	2.7	−12.0	−124.0	30	1.5
16:00 – 16:01	7.5e4	4.1	1.2	2.8	−12.0	−125.0	30	1.4
16:01 – 16:02	7.8e4	4.1	1.2	3.1	−14.0	−125.0	33	1.5
16:02 – 16:03	7.6e4	4.2	1.1	2.5	−13.0	−127.0	31	1.6
16:03 – 16:04	7.7e4	4.1	1.2	2.9	−12.0	−127.0	30	1.5
16:04 – 16:05	7.7e4	4.1	1.1	2.7	−12.0	−127.0	30	1.4
16:05 – 16:06	7.7e4	4.1	1.1	2.7	−12.0	−128.0	33	1.5
16:06 – 16:07	7.7e4	4.1	1.1	2.8	−14.0	−128.0	32	1.5
16:07 – 16:08	7.8e4	4.2	1.2	2.8	−13.0	−131.0	35	1.6
16:08 – 16:08	7.9e4	4.2	1.1	2.7	−13.0	−130.0	37	1.6
16:09 – 16:10	7.9e4	4.3	1.2	2.9	−14.0	−129.0	31	1.5

The intensity of the SEP flux gradually increased during the initial and main phase of the event (roughly corresponding to the prompt component (Vashenyuk et al., 2008)), reaching its peak at 18:15 UT (DOMB maximal count-rate increase of about 14%), and decreased afterwards.

We assess the quality of the fit by comparison between the modeled and the experimentally measured NM count-rate increases. Selected stations are presented in Figure 4. We note that the quality of the fit is similar for the other NM stations.

Similarly to Mishev et al. (2021b), we present in Figure 5 the contour plot of the sum of variances for the best-fit solutions vs. geographic coordinates. Here, the forward modeling is performed over all the possible apparent source positions. We emphasize that an erroneous apparent source-position determination would distort the derived PADs and spectra (see the discussion in Mishev et al., 2021a). One can see that the results of the forward modeling are satisfactory, i.e. the derived solutions are of reasonable quality, implying that the model well described the experimental NM records. Note that the derived apparent source position does not coincide exactly with the minimum of $\mathcal{D}$ because we employed additional fit-quality criteria as discussed in Mishev et al. (2021a,b).

The possibility to fit the SEP spectra with an exponential rigidity spectrum, assuming the same single-Gaussian PAD as derived above, was also examined, details are given in Table 4, and accordingly with the 1-min resolution in Table 5. In this case, the residual, i.e. $\mathcal{D}$ was greater compared to the previous case, specifically after the event onset, that is during the main and late phase, yet during the initial phase of the event, the goodness of fit was of the same order. Therefore, during the event initial phase, the SEP spectra could be fitted with either a modified power law with considerable roll-off or an exponential rigidity spectrum. We note that after 17:00 UT, the only possibility to describe the SEP spectra was with a modified power-law rigidity spectrum, since assuming an exponent rigidity spectrum led to $\mathcal{D} \approx 40 - 50\%$.
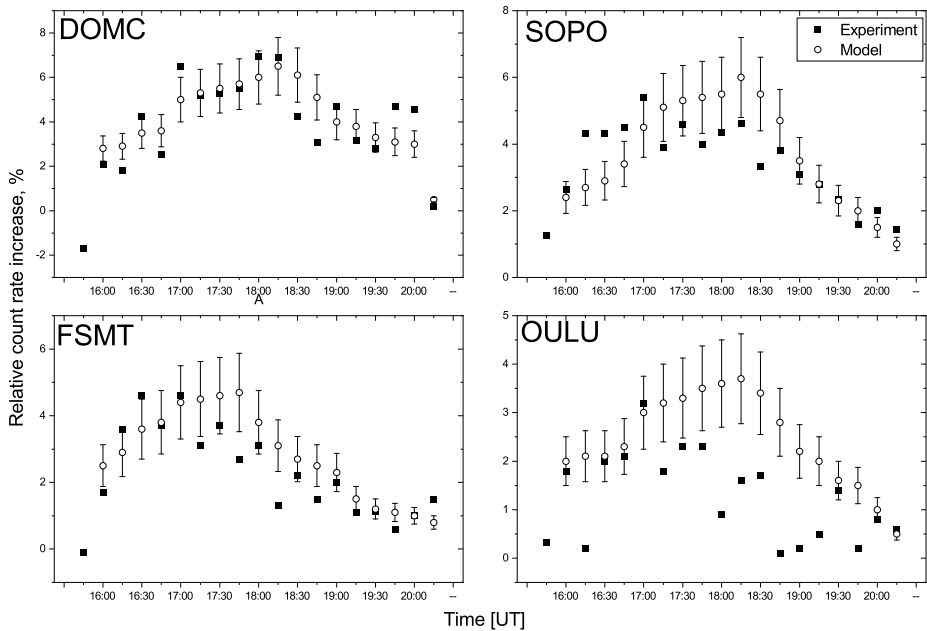
Figure 4 Modeled and measured count-rate increases for selected stations during the GLE N° 73 on 28 October 2021 as depicted in the legend. The error bars correspond to the confidence interval of the solution at level 95% and encompass all the model uncertainties. The quality of the fit for other stations is of the same order.

Figure 5 Contour plot of $\mathcal{D}$ for the best-fit solutions vs. geographic latitude and longitude during the initial phase of GLE N° 73, that was at 16:30 UT. The small white circle depicts the derived apparent source position, the cross depicts the IMF direction measured by ACE satellite.
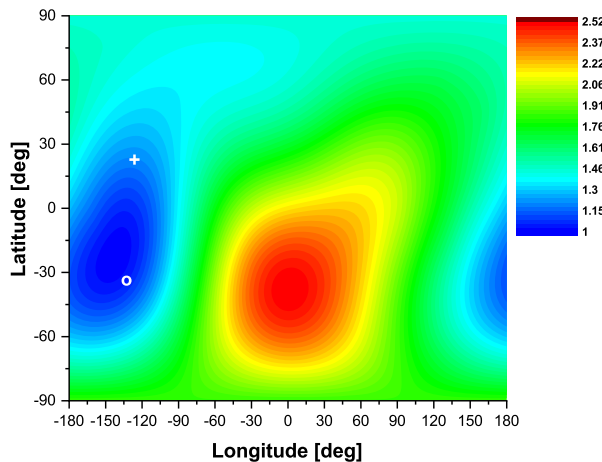
The particle fluence (the time and angle integrated intensity of protons) of GLE N°73 is presented in Figure 6. It is compared with the fluence reconstruction employing the "fast" method (details given in Koldobskiy, Kovaltsov, and Usoskin, 2018; Koldobskiy et al., 2019a; Usoskin et al., 2020). This method allows us to consider each NM as an integrating detector such that its SEP-related count rate is directly proportional to the SEP fluence at some rigidity P (assumed to be constant for a given NM). This method allows us to perform

Table 4 Derived spectral and angular characteristics for GLE N°73 using the exponential rigidity spectrum.

Integration interval UT	J_0 [m^{-2} s^{-1} sr^{-1} GV^{-1}]	P_0 [GV]	σ^2 [rad^2]	Ψ [degrees]	Λ [degrees]	$\mathcal{D}$ [%]	χ_r^2
15:55 – 16:00	1.85e5	0.28	2.8	−10.0	−124	23	1.4
16:00 – 16:05	2.25e5	0.28	2.8	−12.0	−127	18	1.2
16:05 – 16:10	2.27e5	0.29	2.8	−13.0	−187	22	1.3
16:10 – 16:15	2.30e5	0.30	2.9	−14.0	−130	20	1.3
16:15 – 16:20	2.32e5	0.31	2.9	−15.0	−131	16	1.3
16:20 – 16:25	2.33e5	0.31	3.0	−21.0	−132	15	1.3
16:25 – 16:30	2.34e5	0.31	3.1	−30.0	−132	16	1.2
16:30 – 16:35	2.35e5	0.30	3.1	−34.0	−135	14	1.2
16:35 – 16:40	2.36e5	0.31	3.2	−31.0	−137	19	1.4
16:40 – 16:45	2.37e5	0.32	3.3	−35.0	−140	21	1.5

Table 5 Derived spectral and angular characteristics using the exponential rigidity spectrum with 1-minute time resolution during the event onset of GLE N° 73.

Integration interval UT	J_0 [m^{-2} s^{-1} sr^{-1} GV^{-1}]	P_0 [GV]	σ^2 [rad^2]	Ψ [degrees]	Λ [degrees]	$\mathcal{D}$ [%]	χ_r^2
15:55 – 16:56	1.78e5	0.28	2.1	−10.0	−124	27	1.5
15:56 – 16:57	1.81e5	0.28	1.8	−10.0	−124	29	1.6
15:57 – 16:58	1.98e5	0.28	2.0	−12.0	−125	28	1.6
15:58 – 16:59	2.01e5	0.28	2.7	−8.0	−124	31	1.6
15:59 – 16:00	2.12e5	0.28	2.7	−12.0	−124	33	1.6
16:00 – 16:01	2.15e5	0.28	2.8	−12.0	−125	31	1.5
16:01 – 16:02	2.18e5	0.28	3.1	−14.0	−125	32	1.6
16:02 – 16:03	2.21e5	0.28	2.5	−13.0	−127	33	1.6
16:03 – 16:04	2.25e5	0.28	2.9	−12.0	−127	33	1.6
16:04 – 16:05	2.26e5	0.28	2.7	−12.0	−127	32	1.6
16:05 – 16:06	2.27e5	0.29	2.7	−12.0	−128	34	1.6
16:06 – 16:07	2.27e5	0.29	2.8	−14.0	−128	35	1.5
16:07 – 16:08	2.28e5	0.29	2.8	−13.0	−131	26	1.6
16:08 – 16:09	2.29e5	0.29	2.7	−13.0	−130	36	1.6
16:09 – 16:10	2.29e5	0.29	2.9	−14.0	−129	37	1.6

a robust reconstruction of the fluence during GLEs, when studying temporal and spatial features is impossible, this is so because the approach does not consider the anisotropy nor the evolution of GLE characteristics throughout the event. One can see that the fluence obtained with the "fast" analysis method agrees well with the full reconstruction.

Figure 6 SEP fluence for GLE N°73 reconstructed with two methods of analysis: fast and full (see the details in the text), as depicted in the legend. The red and blue filled areas depict the 95% confidence limit for full and fast analysis, respectively.
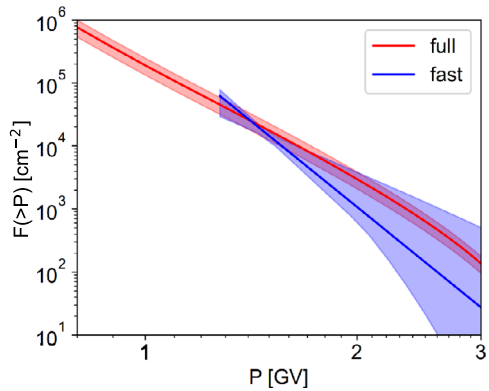
5. Moments of the Fitted Proton Distribution

The available set of counting-rate profiles of the NM network is fitted with the intensity of arriving solar protons according to Equations 2 and 5:

$$j(P, \alpha, t) = J_0 \exp(-\alpha^2/\sigma^2) \, P^{-(\gamma + \delta\gamma(P-1))}, \tag{6}$$

where the pitch angle α is measured from the axis of symmetry of the intensity distribution. The axis direction is determined in geographic coordinates, which is the instrument coordinate system of the NM network (Table 2), while for convenience of data interpretation, here we depict the axis direction in GSE coordinates (Figures 7(b) and (c)).

The zero-order moment of the intensity distribution $j(P, \alpha, t)$ is the omnidirectional intensity:

$$J(P, t) = 2\pi \int_0^\pi j(P, \alpha, t) \sin(\alpha) \, d\alpha. \tag{7}$$

It is proportional to the proton number density $N(P, t) = J(P, t)/v(P)$, where $v(P)$ is proton speed. The number density of 1 GV protons is shown in Figure 7e. It reaches a maximum value in about 2.5 hours after the event onset.

The next moment is the proton net flux:

$$S(P, t) = 2\pi \int_0^\pi j(P, \alpha, t) \cos(\alpha) \sin(\alpha) \, d\alpha, \tag{8}$$

which is relevant to the proton-production profile at the Sun and is also affected by the interplanetary transport. The time profile of the proton net flux is plotted in Figure 7a. The time evolution of the spectrum slope $\delta\gamma$, which is responsible for the spectrum steepening with increase of rigidity, is shown with a color scale. In the late phase of the event, the spectrum is a pure power law, that is $\delta\gamma = 0$, typical for the delayed component of the GLE in contrast to the prompt component typically dominating the initial phase of the events (e.g. Vashenyuk et al., 2006).

In panels b and c of Figure 7, we present the GSE latitude ψ and longitude λ, of the direction of the proton flux arrival. We also plot the IMF direction, as measured by the ACE spacecraft (Smith et al., 1998) but shifted in time by the solar-wind transit time from the probe to the Earth's orbit. In Figure 7b, the R_L bar additionally illustrates the passage time

of a solar-wind structure of the Larmor radius scale of 1 GV protons, $T_L = R_L/U_{sw}$, with $U_{sw} = 300 \text{ km s}^{-1}$ and $B = 4.5$ nT. During the first ≈ 2.5 hours of the event, the magnetic-field direction exhibited strong variations, including a switchback at $t \approx 160$ min, while the direction of the proton flux, S, turned smoothly to the south of the ecliptic plane, and then returned back. In Figure 7d we plot the mean angle between the proton flux axis and the magnetic field, $\langle \alpha_{SB} \rangle$. The mean value was obtained via temporal averages of α_{SB} over a sliding time window extending from the current time t to the time $t + 2R_L/U_{sw}$ (the bar over $\langle \alpha_{SB} \rangle$ illustrates the averaging time scale). The $S{-}B$ (proton flux–magnetic field) angle increased from $\approx 50°$ at the beginning of the event to $90°$ at the flux-maximum time and then returned back. Thus, the GLE-producing solar protons arrived at the vicinity of Earth largely via the crossfield transport, perhaps from southern solar locations.

The average pitch-angle cosine of the GLE-producing solar protons, $\langle \cos(\theta) \rangle = S(P, t)/J(P, t)$, characterizes the proton streaming, relevant to actual interplanetary transport conditions. This is shown in Figure 7e. The observed anisotropy was moderate, even at the beginning of the event, as discussed above.

The last moment shown here is Q, which is the cumulative net flux of energy E up to current time, i.e. fluence of energy of > 1 MV solar protons passing the Earth's orbit:

$$Q(t) = \int_0^t d\tau \int_{1\,\text{MV}}^{\infty} dP \, E(P)S(P, \tau). \tag{9}$$

It can be used as a measure of the GLE power as well as the relative power of its phases. For the time interval shown in Figure 7, 90% of the total energy fluence is accounted for by the prompt component emission.

6. Comparison with SOHO/ERNE Data

An event associated with GLE N° 73 SEP was observed by the ERNE instrument on board the SOHO spacecraft, which is a platform stabilized in such a way that the particle instrument axis points in the ecliptic plain at the GSE longitude either $\lambda = 45°$, either $\lambda = -45°$. On 28 October 2021 the orientation was at $\lambda = -45°$ (45°W). The High Energy Detector (HED) of SOHO/ERNE has a 120°-wide field of view, hence covering the plane of the ecliptic in the sector $-105° \leq \lambda \leq 15°$, therefore provides angular measurements of the particles outside the geomagnetosphere (Torsti et al., 1995).

In Figure 8, we compare the particle data of ERNE on board SOHO and NMs on Earth, on the one hand, and the ACE magnetic-field measurements on the other hand. In the solar-wind flow, the SOHO is orbiting upstream of the ACE, while the Earth is downstream. For comparison sake of Figure 8, we shifted the ERNE data to a later time by the SOHO-ACE transit time of the solar wind, while the NM profiles are shifted to an earlier time by the solar-wind transit time from the ACE to the Earth's orbit.

Based on magnetic-field data, we selected several time intervals, i.e. t_1, t_2, and t_3 (Figure 8). The SEP rise was observed in the time interval t_2–t_3, when the interplanetary magnetic field was inside the ERNE/HED field of view (panel c). The rise phase of a deka-MeV proton event exhibited a clear velocity dispersion corresponding to a traveled distance of $\approx 1.2 - 1.5$ AU (panel a). Then, during the time interval from 215 min to ≈ 245 min, a decrease was observed in all energy channels, implying the spacecraft entered a distinct magnetic flux tube filled with a different particle population. Shortly after the appearance of the distinct proton population, at around time t_3, the magnetic-field magnitude and direction
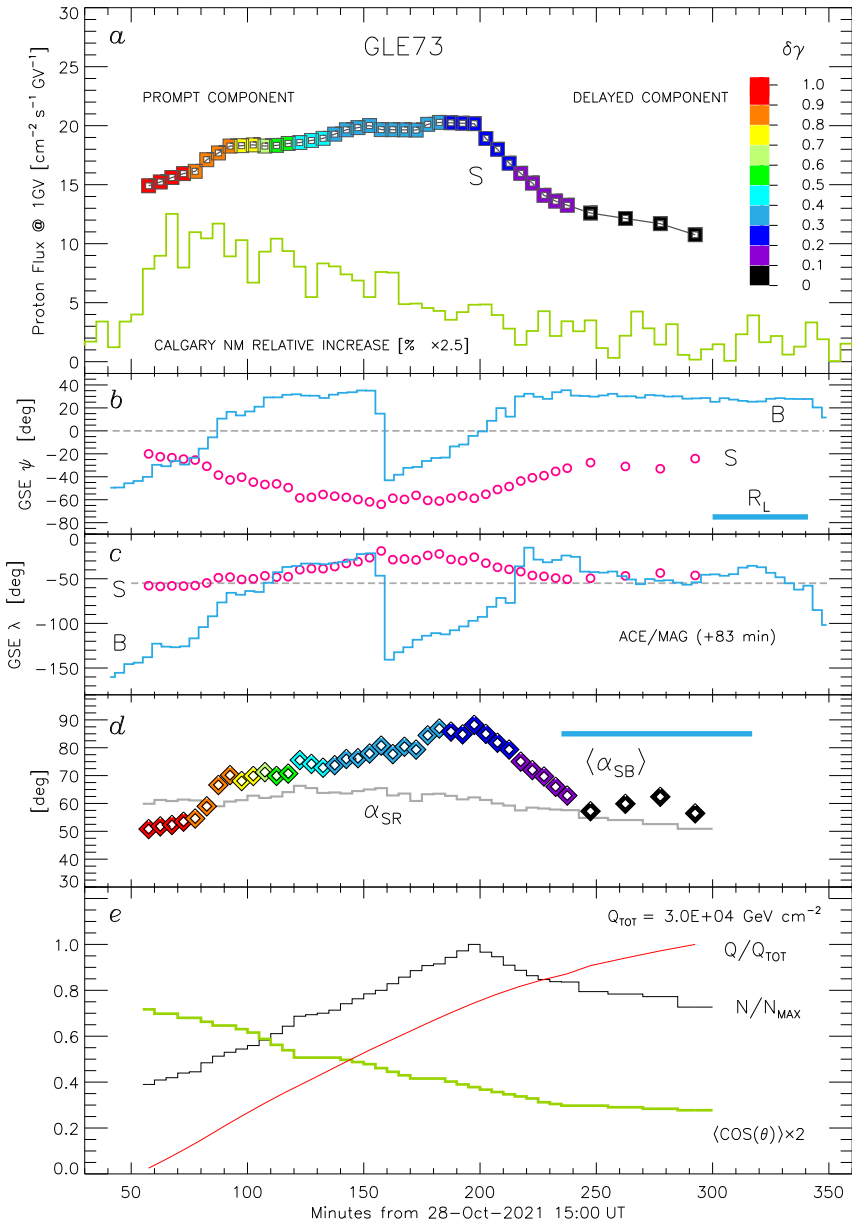
Figure 7 Parameters and moments of the fitted solar proton intensity $j(P, \theta, t)$. (*a*): Net flux of the GLE-producing solar protons, *S*, and a sample of the NM counting-rate profile. (*b*, *c*): GSE angles of the direction the proton flux *S* arrives from latitude ψ and longitude λ, and the direction of interplanetary magnetic field *B* (4-minute data by ACE/MAG). (*d*): Average angle between the proton flux *S* and magnetic field *B*, $\langle \alpha_{SB} \rangle$. Additionally shown is the angle between the flux *S* and the radial, Earth–Sun direction, α_{SR}. (*e*): Average pitch-angle cosine of arriving protons, $\langle \cos(\theta) \rangle$, the number density of 1 GV protons, *N*, the commutative energy fluence of the >1 GV protons, *Q*, and its value at the end of the analyzed period, Q_{TOT}. Dashed lines in panels b and c indicate the direction of the standard, spiral magnetic field of the 300 km s^{-1} solar wind. The scale bars in panels b and d, respectively, are for the proton Larmor radius over the solar-wind speed and the averaging time of the S–B angle.

changed (Figure 8b and c). Those changes may indicate an alteration of magnetic connection to the SEP source apparently situated at the western flank of the CME shock.

The GLE rise and maximum phase were observed in a very different magnetic environment (Figure 8b–e). At around the maximum intensity of the GLE-producing solar protons, from t_1 to t_2, the interplanetary magnetic field dramatically deviated from the standard, spiral field direction, while the GV proton flux did not follow those fast changes, apparently because of the large Larmor radius of the GV protons.

For further comparison of the NM data with ERNE data, we created a virtual GV proton channel of ERNE/HED by sampling the GLE protons in the HED viewing cone, $\Delta\Omega_{\text{HED}}$, that is a circular cone of 60° half-width with axis in the ecliptic plane pointing at $\lambda = -45°$:

$$\langle j(P,t)\rangle_{\text{HED}} = \frac{dP/dE}{\Delta\Omega_{\text{HED}}} \int_{\Delta\Omega_{\text{HED}}} j(P,\theta,t)d\Omega. \tag{10}$$

In Figure 9, such a channel profile is compared with the HED-observed profiles of deka-MeV protons.

All profiles of Figure 9 are shifted back in time to a near-Sun particle source by subtracting the time it takes a proton to travel the distance of 1.4 AU, and then adding 8 minutes for possible comparison with data of solar electromagnetic emissions. It can be seen that the time–intensity profile of GeV protons is very different from the common profile of the deka-MeV protons. Note that the time-shifting technique is a kind of velocity-dispersion analysis and cannot completely deconvolve the interplanetary transport effect, especially after the event rise phase (e.g. Kocharov et al., 2015).

HED of SOHO/ERNE comprises both silicon detectors and a scintillator, allowing proton-flux anisotropy measurements in the deka–MeV energy range. For the present analysis of the proton-flux anisotropy, we divide the field of view of HED into the five sectors shown in the inset of Figure 10. Time–intensity profiles of protons in those sectors are plotted in panel a. In panel b, intensities observed in opposite sectors are compared using two anisotropy indices, $A_{\text{NORTH–SOUTH}}$ and $A_{\text{SUN–WEST}}$, defined in the figure.

For comparison, in Figure 10c, we plot similar indices calculated for the GLE-producing protons arriving within the field of view of HED. The GV proton distribution, $j(P,\alpha,t)$, has been integrated over the following five sectors: (1) Zenith cone with axis along the GSE direction ($\lambda = -45°$, $\psi = 0°$), with opening half-angle of 30°. (2) North lobe covering the GSE latitudes ψ from 30° to 60°, within the field of view of HED. (3) South lobe extending from $\psi = -30°$ to $-60°$. (4) Sunward lobe covering the sector $-30° < \psi < 30°$ east of the Zenith cone. (5) West lobe within $-30° < \psi < 30°$ west of the Zenith cone.

In the 28 October 2021 SEP/GLE event, the anisotropy of relativistic protons was surprisingly low compared to the anisotropy of deka–MeV protons. The anisotropy direction in the deka–MeV range and the anisotropy direction in the GeV range were also different. At lower energies, more particles arrived from the north and west, consistently with the observed direction of the interplanetary magnetic field (Figure 8). In contrast, the relativistic protons arrived preferentially from the south, similarly to the eruption center location on the solar disk.

7. Discussion and Conclusion

In the analysis presented here, we derived the spectral and angular shapes of high-energy SEPs during the first GLE event of Solar Cycle 25, namely GLE N° 73 that occurred on 28
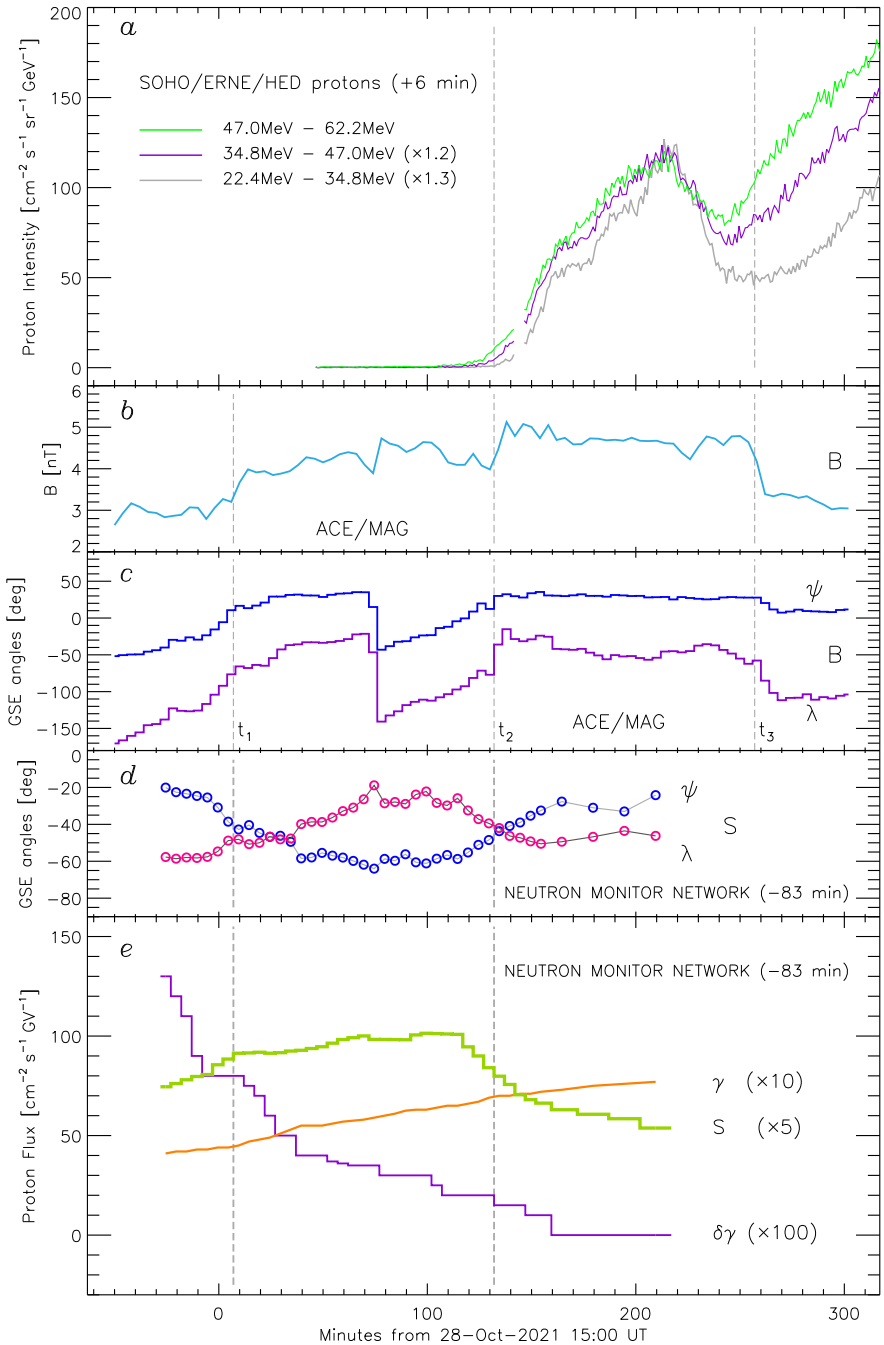
Figure 8 Solar energetic particles in relation with the ACE/MAG-observed structure of the interplanetary magnetic field. (*a*): Deka – MeV proton profiles in three energy channels of SOHO/ERNE (shifted by the solar-wind transit time from the SOHO orbit to the orbit of ACE). (*b*, *c*): Interplanetary magnetic-field intensity and direction observed by ACE. (*d*, *e*): Characteristics of the GLE-producing protons deduced from the NM data (same as in Figure 7 but shifted back by the ACE-Earth solar-wind transit time).
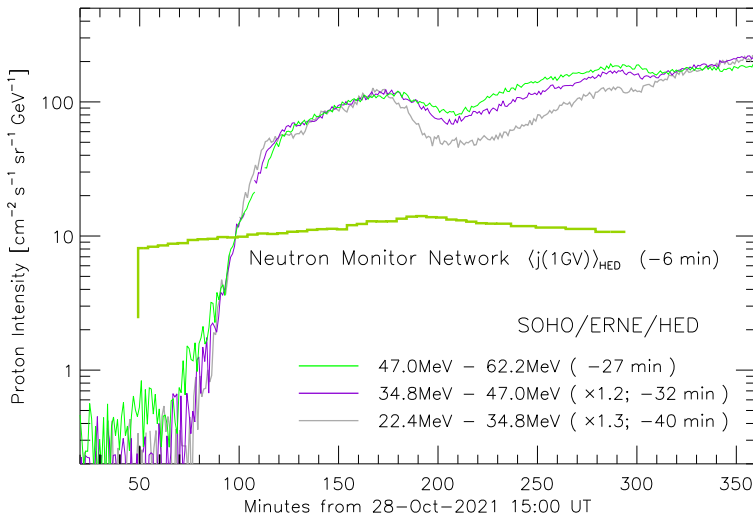
Figure 9 Time-shifted profiles of the HED-detected protons and the GLE profile converted to the HED field of view (Equation 10).

October 2021. The detailed modeling of the global NM network response and the application of a method verified by direct space-borne measurements, allowed us to obtain precise information about the spectra of the SEPs with the best possible time resolution (1 minute during the event onset) available from the existing data sets, thus revealing with high resolution the characteristics of the prompt component and with lower resolution the delayed component. Several possible shapes of the spectra and PAD were studied, and the best fit was achieved with a modified power law in the spectra and a single Gaussian as the angular distribution, yet satisfactory results were obtained with an exponential rigidity spectrum for the prompt component. We revealed that the rigidity spectra were moderately hard ($\gamma \approx 4.5$) during the event initial phase with a significant steeping $\delta\gamma \approx 1.1$, which constantly decreased throughout the later stages of the event. The derived SEP spectra gradually softened during the event. Accordingly, the derived PAD was relatively wide in contrast to the two previous GLEs, namely with a distribution width σ^2 of about π. The revealed angular distribution may be a result of a perpendicular transport of the SEPs (e.g. Kocharov et al., 2005; Ruffolo et al., 2008), however, a more detailed modeling turns out to be necessary, and is planned as forthcoming work.

The uncertainties of the derived characteristics were explicitly assessed, and were larger than those for the previous weak GLEs N° 72, namely of the order of 30% for the spectra and PAD and about 15 degrees for the apparent source position, most likely due to larger NM count-rate fluctuations. The assessed confidence limits of the spectra and PAD were slightly greater than the systematic errors of the employed NM yield function, i.e. those related to the atmospheric cascade evolution (e.g. Alves Batista et al., 2019, and references therein).

The velocity-dispersion magnitude observed in the deka–MeV proton channels of ERNE/HED corresponded to the traveled distance of ≈ 1.4 AU. The average distance traveled by particles from the source to the detector depended on the magnetic line length and interplanetary scattering conditions. A traveled distance as small as 1.4 AU allowed only a weak scattering of deka–MeV protons to exist between the Sun and the Earth, corresponding to the proton mean free path $\Lambda_\parallel > 2.5$ AU (Figure 1 of Kocharov et al., 2015). How-
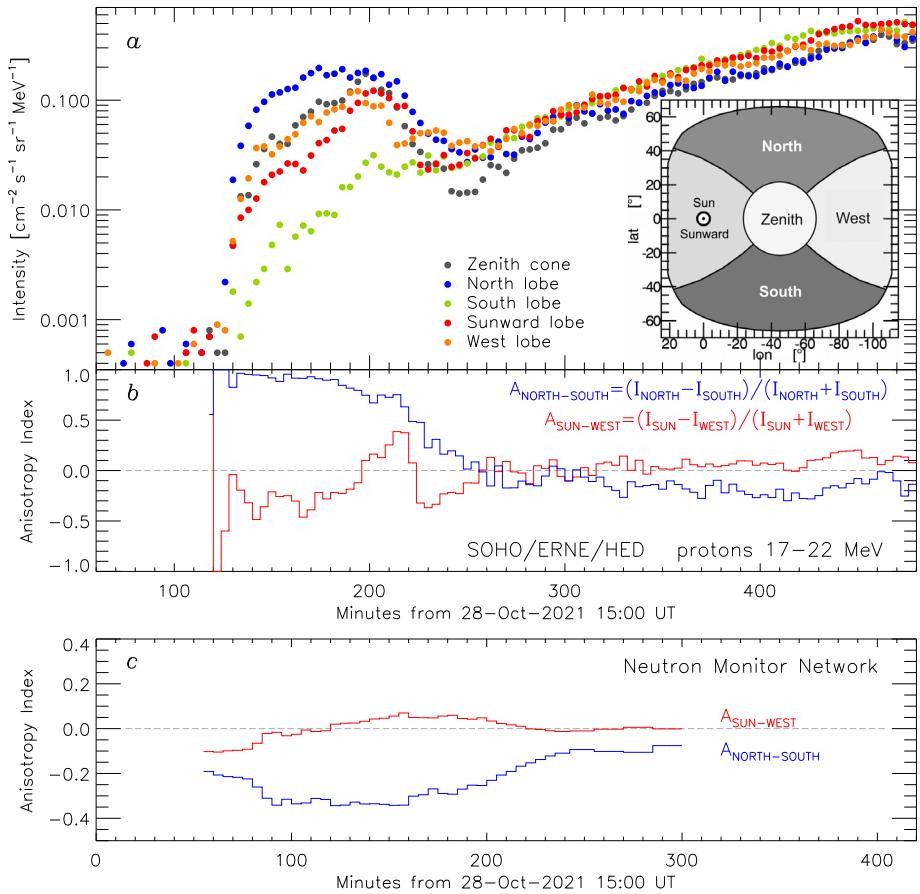
Figure 10 Sectoral intensities of the ERNE/HED-observed protons, their anisotropy indices, and anisotropy indices of GeV protons observed by the NM Network. (*a*): The $17-22$ MeV proton-intensity profiles in five angular sectors of the field of view of HED (the sectors are defined in the instrument reference frame as shown in the inset). (*b*): Anisotropy indices of the ERNE-observed protons. (*c*): Anisotropy indices of GLE-producing protons (for angular sectors explained in the text).

ever, no strong anisotropy was seen in NM data: the average pitch-angle cosine of arriving high-energy protons $\langle \cos(\theta) \rangle \leq 0.35$ (Figure 7e). This may be explained by the GV-proton transport across magnetic-field lines with corresponding mean free path $\Lambda_\perp < \Lambda_\parallel$. The latter implied a larger value of traveled distance and correspondingly, a somewhat earlier injection time of the 1 GV protons compared to the timing shown in Figure 9.

By the onset time of the ERNE-observed deka–MeV proton emission, $\approx 16{:}10$ UT, the CME had already expanded to heliocentric distances $> 4R_\odot$, so the deka–MeV protons could be accelerated by the CME shock in the solar wind. In contrast, emission of the NM-observed high-energy protons started before 15:50 UT. At that time, the CME was still low in the corona, below $1.5R_\odot$ above the chromosphere. This supports the idea of a coronal origin of the prompt component of GLE event(s).

The study and related discussion presented here give a reliable basis for understanding the nature of high-energy SEPs as well as for quantifying the corresponding space-weather effects (e.g. Jiggens et al., 2019).

Data Availability The datasets generated during and/or analyzed during the current study are available on the corresponding web-pages of the space-borne instruments, while the NM records are available in the International GLE Database https://gle.oulu.fi.

Declarations

Disclosure and Potential Conflicts of Interest The authors declare that they have no conflicts of interest.

References

Adriani, O., Barbarino, G.C., Bazilevskaya, G.A., Bellotti, R., Boezio, M., Bogomolov, E.A., et al.: 2015, Pamela's measurements of magnetospheric effects on high-energy solar particles. *Astrophys. J. Lett.* **801**(1), L3. DOI.

Adriani, O., Barbarino, G.C., Bazilevskaya, G.A., Bellotti, R., Boezio, M., Bogomolov, E.A., et al.: 2017, Ten Years of PAMELA in Space. *Riv. Nuovo Cimento* **40**(10), 473. DOI.

Aguilar, M., Ali Cavasonza, L., Ambrosi, G., Arruda, L., Attig, N., Barao, F., et al.: 2021, The Alpha Magnetic Spectrometer (AMS) on the international space station: Part II" Results from the first seven years. *Phys. Rep.* **894**, 1. DOI.

Aleksandrov, L.: 1971, The Newton-Kantorovich regularized computing processes. *U.S.S.R. Comput. Math. Math. Phys.* **11**(1), 46. DOI.

Alken, P., Thébault, E., Beggan, C.D., Amit, H., Aubert, J., Baerenzung, J., et al.: 2021, International geomagnetic reference field: the thirteenth generation. *Earth Planets Space* **73**(1), 49. DOI.

Alves Batista, R., Biteau, J., Bustamante, M., Dolag, K., Engel, R., Fang, K., et al.: 2019, Open questions in cosmic-ray research at ultrahigh energies. *Front. Astron. Space Sci.* **6**, 23. DOI.

Anastasiadis, A., Lario, D., Papaioannou, A., Kouloumvakos, A., Vourlidas, A.: 2019, Solar energetic particles in the inner heliosphere: Status and open questions. *Phil. Trans. Roy. Soc., Math. Phys. Eng. Sci.* **377**(2148), 20180100. DOI.

Aschwanden, M.: 2012, GeV particle acceleration in solar flares and ground level enhancement (gle) events. *Space Sci. Rev.* **171**(1–4), 3.

Aster, R.C., Borchers, B., Thurber, C.H.: 2005, *Parameter estimation and inverse problems*, Elsevier, New York. 0-12-065604-3.

Bieber, J.W., Evenson, P.A.: 1995, Spaceship earth - an optimized network of neutron monitors. In: *Proc. of 24th ICRC* **4**, 1316.

Bieber, J.W., Clem, J., Evenson, P., Pyle, R., Sáiz, A., Ruffolo, D.: 2013, Giant ground level enhancement of relativistic solar protons on 2005 January 20. I. Spaceship earth observations. *Astrophys. J.* **771**(2), 92. DOI.

Bombardieri, D.J., Duldig, M.L., Michael, K.J., Humble, J.E.: 2006, Relativistic proton production during the 2000 July 14 solar event: The case for multiple source mechanisms. *Astrophys. J.* **644**(1), 565.

Bombardieri, D.J., Michael, K.J., Duldig, M.L., Humble, J.E.: 2007, Relativistic proton production during the 2001 April 15 solar event. *Astrophys. J.* **665**(1 Part 1), 813. DOI.

Brueckner, G.E., Howard, R.A., Koomen, M.J., Korendyke, C.M., Michels, D.J., Moses, J.D., et al.: 1995, The large angle spectroscopic coronagraph (lasco) - visible light coronal imaging and spectroscopy. *Solar Phys.* **162**(1–2), 357. DOI.

Bruno, A., Bazilevskaya, G.A., Boezio, M., Christian, E.R., Nolfo, G.A.D., Martucci, M., et al.: 2018, Solar energetic particle events observed by the PAMELA mission. *Astrophys. J.* **862**(2), 97. DOI.

Bruno, A., Christian, E.R., de Nolfo, G.A., Richardson, I.G., Ryan, J.M.: 2019, Spectral analysis of the September 2017 solar energetic particle events. *Space Weather* **17**(3), 419. DOI.

Bütikofer, R., Flückiger, E.O., Desorgher, L., Moser, M.R., Pirard, B.: 2009, The solar cosmic ray ground-level enhancements on 20 January 2005 and 13 December 2006. *Adv. Space Res.* **43**(4), 499.

Clem, J., Dorman, L.: 2000, Neutron monitor response functions. *Space Sci. Rev.* **93**, 335.

Cliver, E.W.: 2016, Flare versus shock acceleration of high-energy protons in solar energetic particle events. *Astrophys. J.* **832**(2), 128. DOI.

Cooke, D.J., Humble, J.E., Shea, M.A., Smart, D.F., Lund, N., Rasmussen, I.L., et al.: 1991, On cosmic-ray cutoff terminology. *Il Nuovo Cimento C* **14**(3), 213.

Cramp, J.L., Humble, J.E., Duldig, M.L.: 1995, The cosmic ray ground-level enhancement of 24 October 1989. In: *Proc. Astron. Soc. Australia* **11**, 28.

Cramp, J.L., Duldig, M.L., Flückiger, E.O., Humble, J.E., Shea, M.A., Smart, D.F.: 1997, The October 22, 1989,solar cosmic enhancement: ray an analysis the anisotropy spectral characteristics. *J. Geophys. Res.* **102**(A11), 24,237.

Debrunner, H., Flückiger, E.O., Gradel, H., Lockwood, J.A., McGuire, R.E.: 1988, Observations related to the acceleration, injection, and interplanetary propagation of energetic protons during the solar cosmic ray event on February 16, 1984. *J. Geophys. Res.* **93**(A7), 7206.

Dennis, J.E., Schnabel, R.B.: 1996, *Numerical methods for unconstrained optimization and nonlinear equations*, Prentice-Hall, Englewood Cliffs. 13-978-0-898713-64-0.

Desai, M., Giacalone, J.: 2016, Large gradual solar energetic particle events. *Living Rev. Solar Phys.* **13**(1), 3. DOI.

Dorman, L.: 2004, *Cosmic rays in the Earth's atmosphere and underground*, Kluwer Academic, Dordrecht, 1 1-4020-2071-6.

Ellison, D.C., Ramaty, R.: 1985, Shock acceleration of electrons and ions in solar flares. *Astrophys. J.* **298**, 400. DOI.

Golub, G.H., Van Loan, C.F.: 1980, An analysis of the total least squares problem. *SIAM J. Numer. Anal.* **17**(6), 883.

Golub, G.H., Hansen, P.C., O'Leary, D.P.: 1999, Tikhonov regularization and total least squares. *SIAM J. Matrix Anal. Appl.* **21**, 185.

Gopalswamy, N., Xie, H., Akiyama, S., Mäkelä, P.A., Yashiro, S.: 2014, Major solar eruptions and high-energy particle events during solar cycle 24. *Earth Planets Space* **66**(1), 104. DOI.

Hatton, C.: 1971, The neutron monitor. In: *Progress in Elementary Particle and Cosmic-ray Physics X*, North Holland Publishing Co., Amsterdam. Chapter 1.

Himmelblau, D.M.: 1972, *Applied nonlinear programming*. Mcgraw-Hill(Tx), Texas 978-0070289215.

Jiggens, P., Clavie, C., Evans, H., O'Brien, T.P., Witasse, O., Mishev, A.L., et al.: 2019, In situ data and effect correlation during September 2017 solar particle event. *Space Weather* **17**(1), 99. DOI.

Klein, K.-L., Dalla, S.: 2017, Acceleration and propagation of solar energetic particles. *Space Sci. Rev.* **212**(3–4), 1107. DOI.

Klein, K.-L., Trottet, G.: 2001, The origin of solar energetic particle events: Coronal acceleration versus shock wave acceleration. *Space Sci. Rev.* **95**, 215.

Kocharov, L., Kovaltsov, G., Torsti, J., Huttunen-Heikinmaa, K.: 2005, Modeling the solar energetic particle events in closed structures of interplanetary magnetic field. *J. Geophys. Res.* **110**(A12), A12S03.

Kocharov, L., Klassen, A., Valtonen, E., Usoskin, I., Ryan, J.M.: 2015, Comparative morphology of solar relativistic particle events. *Astrophys. J. Lett.* **811**(1), L9. DOI.

Kocharov, L., Pohjolainen, S., Reiner, M.J., Mishev, A., Wang, H., Usoskin, I., Vainio, R.: 2018, Spatial organization of seven extreme solar energetic particle events. *Astrophys. J. Lett.* **862**(2), L20. DOI.

Kocharov, L., Pesce-Rollins, M., Laitinen, T., Mishev, A., Kühl, P., Klassen, A., et al.: 2020, Interplanetary protons versus interacting protons in the 2017 September 10 solar eruptive event. *Astrophys. J.* **890**(1), 13. DOI.

Kocharov, L., Omodei, N., Mishev, A., Pesce-Rollins, M., Longo, F., Yu, S., et al.: 2021, Multiple sources of solar high-energy protons. *Astrophys. J.* **915**(1), 12. DOI.

Koldobskiy, S.A., Kovaltsov, G.A., Usoskin, I.G.: 2018, Effective Rigidity of a Polar Neutron Monitor for Recording Ground-Level Enhancements. *Solar Phys.* **293**(7), 110. DOI.

Koldobskiy, S.A., Kovaltsov, G.A., Mishev, A.L., Usoskin, I.G.: 2019a, New method of assessment of the integral fluence of solar energetic (> 1 GV rigidity) particles from neutron monitor data. *Solar Phys.* **294**(7), 94. DOI.

Koldobskiy, S.A., Bindi, V., Corti, C., Kovaltsov, G.A., Usoskin, I.G.: 2019b, Validation of the neutron monitor yield function using data from AMS-02 experiment, 2011–2017. *J. Geophys. Res. Space Phys.* **124**(4), 2367. DOI.

Koldobskiy, S., Raukunen, O., Vainio, R., Kovaltsov, G.A., Usoskin, I.: 2021, New reconstruction of event-integrated spectra (spectral fluences) for major solar energetic particle events. *Astron. Astrophys.* **647**, A132. DOI.

Kudela, K., Usoskin, I.: 2004, On magnetospheric transmissivity of cosmic rays. *Czechoslov. J. Phys.* **54**(2), 239.

Kudela, K., Bučik, R., Bobik, P.: 2008, On transmissivity of low energy cosmic rays in disturbed magnetosphere. *Adv. Space Res.* **42**(7), 1300.

Kühl, P., Dresing, N., Heber, B., Klassen, A.: 2017, Solar energetic particle events with protons above 500 MeV between 1995 and 2015 measured with SOHO/EPHIN. *Solar Phys.* **292**(1), 10. DOI.

Lara, A., Borgazzi, A., Caballero-Lopez, R.: 2016, Altitude survey of the galactic cosmic ray flux with a mini neutron monitor. *Adv. Space Res.* **58**(7), 1441. DOI.

Levenberg, K.: 1944, A method for the solution of certain non-linear problems in least squares. *Q. Appl. Math.* **2**, 164.

Marquardt, D.: 1963, An algorithm for least-squares estimation of nonlinear parameters. *SIAM J. Appl. Math.* **11**(2), 431.

Mavrodiev, S.C., Mishev, A.L., Stamenov, J.N.: 2004, A method for energy estimation and mass composition determination of primary cosmic rays at the Chacaltaya observation level based on the atmospheric Cherenkov light technique. *Nucl. Instrum. Methods Phys. Res., Sect. A, Accel. Spectrom. Detect. Assoc. Equip.* **530**(3), 359. DOI.

Mavromichalaki, H., Papaioannou, A., Plainaki, C., Sarlanis, C., Souvatzoglou, G., Gerontidou, M., et al.: 2011, Applications and usage of the real-time neutron monitor database. *Adv. Space Res.* **47**, 2210.

Miroshnichenko, L.I.: 2018, Retrospective analysis of gles and estimates of radiation risks. *J. Space Weather Space Clim.* **8**, A52. DOI.

Mishev, A., Poluianov, S.: 2021, About the altitude profile of the atmospheric cut-off of cosmic rays: New revised assessment. *Solar Phys.* **296**(8), 129. DOI.

Mishev, A., Usoskin, I.: 2016, Analysis of the ground level enhancements on 14 July 2000 and on 13 December 2006 using neutron monitor data. *Solar Phys.* **291**(4), 1225.

Mishev, A., Usoskin, I.: 2020, Current status and possible extension of the global neutron monitor network. *J. Space Weather Space Clim.* **10**, 17. DOI.

Mishev, A.L., Kocharov, L.G., Usoskin, I.G.: 2014, Analysis of the ground level enhancement on 17 May 2012 using data from the global neutron monitor network. *J. Geophys. Res.* **119**, 670.

Mishev, A., Mavrodiev, S., Stamenov, J.: 2005, Gamma rays studies based on atmospheric Cherenkov technique at high mountain altitude. *Int. J. Mod. Phys. A* **20**(29), 7016. DOI.

Mishev, A., Poluianov, S., Usoskin, S.: 2017, Assessment of spectral and angular characteristics of sub-gle events using the global neutron monitor network. *J. Space Weather Space Clim.* **7**, A28. DOI.

Mishev, A.L., Koldobskiy, S.A., Kovaltsov, G.A., Gil, A., Usoskin, I.G.: 2020, Updated neutron-monitor yield function: Bridging between in situ and ground-based cosmic ray measurements. *J. Geophys. Res. Space Phys.* **125**(2), e2019JA027433. DOI.

Mishev, A., Usoskin, I., Raukunen, O., Paassilta, M., Valtonen, E., Kocharov, L., Vainio, R.: 2018, First analysis of GLE 72 event on 10 September 2017: Spectral and anisotropy characteristics. *Solar Phys.* **293**, 136.

Mishev, A.L., Koldobskiy, S.A., Usoskin, I.G., Kocharov, L.G., Kovaltsov, G.A.: 2021a, Application of the verified neutron monitor yield function for an extended analysis of the GLE # 71 on 17 May 2012. *Space Weather* **19**(2), e2020SW002626. DOI.

Mishev, A.L., Koldobskiy, S.A., Kocharov, L.G., Usoskin, I.G.: 2021b, GLE # 67 event on 2 November 2003: An analysis of the spectral and anisotropy characteristics using verified yield function and detrended neutron monitor data. *Solar Phys.* **296**(5), 79. DOI.

Moraal, H., McCracken, K.G.: 2012, The time structure of ground level enhancements in solar cycle 23. *Space Sci. Rev.* **171**(1–4), 85.

Nevalainen, J., Usoskin, I., Mishev, A.: 2013, Eccentric dipole approximation of the geomagnetic field: Application to cosmic ray computations. *Adv. Space Res.* **52**(1), 22.

Nuntiyakul, W., Sáiz, A., Ruffolo, D., Mangeard, P.-S., Evenson, P., Bieber, J.W., et al.: 2018, Bare neutron counter and neutron monitor response to cosmic rays during a 1995 latitude survey. *J. Geophys. Res. Space Phys.* **123**(9), 7181. DOI.

Nuntiyakul, W., Mangeard, P.-S., Ruffolo, D., Evenson, P., Bieber, J.W., Clem, J., et al.: 2020, Direct determination of a bare neutron counter yield function. *J. Geophys. Res. Space Phys.* **125**(4), e2019JA027304. DOI.

Papaioannou, A., Souvatzoglou, G., Paschalis, P., Gerontidou, M., Mavromichalaki, H.: 2014, The first ground-level enhancement of solar cycle 24 on 17 May 2012 and its real-time detection. *Solar Phys.* **289**(1), 423. DOI.

Papaioannou, A., Kouloumvakos, A., Mishev, A., Vainio, R., Usoskin, I., Herbst, K., et al.: 2022, The first ground level enhancement of solar cycle 25 on 28 October 2021. *Astron. Astrophys.* **660**, L5. DOI.

Plainaki, C., Mavromichalaki, H., Laurenza, M., Gerontidou, M., Kanellakopoulos, A., Storini, M.: 2014, The ground-level enhancement of 2012 may 17: Derivation of solar proton event properties through the application of the nmbangle ppola model. *Astrophys. J.* **785**(2), 160. DOI.

Poluianov, S.V., Usoskin, I.G., Mishev, A.L., Shea, M.A., Smart, D.F.: 2017, GLE and sub-GLE redefinition in the light of high-altitude polar neutron monitors. *Solar Phys.* **292**(11), 176. DOI.

Raukunen, O., Vainio, R., Tylka, A.J., Dietrich, W.F., Jiggens, P., Heynderickx, D., et al.: 2018, Two solar proton fluence models based on ground level enhancement observations. *J. Space Weather Space Clim.* **8**, A04. DOI.

Reames, D.V.: 1999, Particle acceleration at the sun and in the heliosphere. *Space Sci. Rev.* **90**(3–4), 413.

Ruffolo, D., Tooprakai, P., Rujiwarodom, M., Khumlumlert, T., Wechakama, M., Bieber, J.W., Evenson, P.A., Pyle, K.R.: 2006, Relativistic solar protons on 1989 October 22: Injection and transport along both legs of a closed interplanetary magnetic loop. *Astrophys. J.* **639**(2), 1186.

Ruffolo, D., Chuychai, P., Wongpan, P., Minnie, J., Bieber, J.W., Matthaeus, W.H.: 2008, Perpendicular transport of energetic charged particles in nonaxisymmetric two-component magnetic turbulence. *Astrophys. J.* **686**(2), 1231. DOI.

Shea, M.A., Smart, D.F.: 1982, Possible evidence for a rigidity-dependent release of relativistic protons from the solar corona. *Space Sci. Rev.* **32**, 251.

Simpson, J.: 2000, The cosmic ray nucleonic component: The invention and scientific uses of the neutron monitor. *Space Sci. Rev.* **93**, 11. DOI.

Simpson, J., Fonger, W., Treiman, S.: 1953, Cosmic radiation intensity-time variation and their origin. i. neutron intensity variation method and meteorological factors. *Phys. Rev.* **90**, 934.

Smith, C.W., L'Heureux, J., Ness, N.F., Acuña, M.H., Burlaga, L.F., Scheifele, J.: 1998, The ACE magnetic fields experiment. *Space Sci. Rev.* **86**(1–4), 613. DOI.

Stoker, P.H., Dorman, L.I., Clem, J.M.: 2000, Neutron monitor design improvements. *Space Sci. Rev.* **93**(1–2), 361.

Tikhonov, A.N., Goncharsky, A.V., Stepanov, V.V., Yagola, A.G.: 1995, *Numerical methods for solving ill-posed problems*, Kluwer Academic, Dordrecht, 978.

Torsti, J., Valtonen, E., Lumme, M., Peltonen, P., Eronen, T., Louhola, M., et al.: 1995, Energetic particle experiment ERNE. *Solar Phys.* **162**(1–2), 505. DOI.

Tsyganenko, N.A.: 1989, A magnetospheric magnetic field model with a warped tail current sheet. *Planet. Space Sci.* **37**(1), 5.

Usoskin, I., Koldobskiy, S., Kovaltsov, G.A., Gil, A., Usoskina, I., Willamo, T., Ibragimov, A.: 2020, Revised GLE database: Fluences of solar energetic particles as measured by the neutron-monitor network since 1956. *Astron. Astrophys.* **640**, 2038272. DOI.

Vainio, R., Desorgher, L., Heynderickx, D., Storini, M., Flückiger, E., Horne, R.B., et al.: 2009, Dynamics of the earth's particle radiation environment. *Space Sci. Rev.* **147**(3–4), 187.

Vainio, R., Valtonen, E., Heber, B., Malandraki, O.E., Papaioannou, A., Klein, K.-L., et al.: 2013, The first sepserver event catalogue 68-MeV solar proton events observed at 1 AU in 1996-2010. *J. Space Weather Space Clim.* **3**, A12. DOI.

Vashenyuk, E.V., Balabin, Y.V., Stoker, P.H.: 2007, Responses to solar cosmic rays of neutron monitors of a various design. *Adv. Space Res.* **40**(3), 331.

Vashenyuk, E.V., Balabin, Y.V., Perez-Peraza, J., Gallegos-Cruz, A., Miroshnichenko, L.I.: 2006, Some features of the sources of relativistic particles at the sun in the solar cycles 21–23. *Adv. Space Res.* **38**(3), 411.

Vashenyuk, E.V., Balabin, Y.V., Gvozdevsky, B.B., Schur, L.I.: 2008, Characteristics of relativistic solar cosmic rays during the event of December 13. *Geomagn. Aeron.* **48**(2), 149. 2006.

Velinov, P.I.Y.: 2022, Major X-class solar flare from earth-facing active region AR 12887 on October 28, 2021 and first cosmic ray GLE 73 in solar cycle 25. *C. R. Acad. Bulgare Sci.* **75**(2), 248.

Publisher's Note   Springer Nature remains neutral with regard to jurisdictional claims in published maps and institutional affiliations.